Applied Surface Science 737 (2026) 166898

Contents lists available at ScienceDirect

Applied Surface Science

journal homepage: www.elsevier.com/locate/apsusc

Full Length Article

Simultaneous reduction and electrode patterning of TiO_2/GO films via femtosecond laser for UV-enhanced flexible CO gas sensors

Yuan-Jun Chen [a], Tien-Li Chang [a,*], Shih-Feng Tseng [b,*], Wen-Tse Hsiao [c], Shu-Han Hsu [d,*]

[a] Department of Mechatronic Engineering, National Taiwan Normal University, Taipei 106, Taiwan, ROC
[b] Department of Mechanical Engineering, National Taipei University of Technology, Taipei 106, Taiwan, ROC
[c] National Center for Instrumentation Research, National Institutes of Applied Research, Hsinchu 300, Taiwan, ROC
[d] Sirindhorn Institute International of Technology, Thammasat University, Pathum Thani 12120, Thailand

ARTICLE INFO

Keywords:
Femtosecond laser
TiO_2/rGO composite
Flexible CO gas sensor
Laser-induced technology

ABSTRACT

Reliable and sensitive gas sensors are essential for ensuring industrial safety and environmental monitoring. In this study, a flexible carbon monoxide (CO) gas sensor based on titanium dioxide (TiO_2) and reduced graphene oxide (rGO) composite was developed for rapid and highly sensitive detection. The device was fabricated using one-step femtosecond laser (Fs-laser) processing, which simultaneously reduced a TiO_2/graphene oxide (GO) thin film and patterned electrodes directly on a flexible substrate. Optimized laser parameters, including a repetition rate of 100 kHz, a scanning speed of 50 mm/sec, and a fluence of 0.34 J/cm^2, enabled efficient film reduction and ensured reliable device performance. The sensor exhibited an initial response of 39.6% to CO gas at room temperature (25 °C), which was further enhanced to a maximum response of 43.8% under ultraviolet (UV) irradiation. Under 365 nm UV irradiation, the photocatalytic activity of TiO_2 induced a substantial reduction in overall resistance, significantly improving the sensing capability. These findings demonstrate the potential of TiO_2/rGO composite in UV-enhanced flexible CO gas sensors, and provide a promising strategy to improve sensitivity, selectivity, and stability in gas sensing applications.

1. Introduction

Environmental pollution has become an increasingly serious global issue as industrialization and urban development accelerate. Among various forms of pollution, air contamination caused by fossil fuel combustion and industrial gas emissions has attracted significant attention [1]. These harmful gases not only damage the natural ecosystem, but also threaten human lives. Carbon monoxide (CO) is known to be one of the colorless, odorless, and hazardous gas primarily produced during the incomplete combustion of hydrocarbons [2,3]. CO has a binding affinity for hemoglobin that is 230–270 times greater than oxygen [4]. Upon inhalation, it readily replaces oxygen in hemoglobin, significantly impairing the oxygen of the blood transport capacity. This can lead to tissue and organ hypoxia, severe toxic effects, and, in extreme cases, brain damage or death [5]. Thus, the device for CO detection has become a major challenge for scientific researchers, making the real-time monitoring of trace CO concentrations crucial for ensuring safety.

To meet the demand for effective CO detection, numerous materials have been investigated for gas sensing. Among these, graphene, a two-dimensional carbon-based material, has garnered significant attention due to its exceptional electrical properties and large surface area [6,7]. However, its low adsorption efficiency for gas molecules limits its practical application in gas sensors. To address this limitation, reduced graphene oxide (rGO), a derivative of graphene oxide (GO) obtained through chemical or thermal reduction, has emerged as a promising alternative. rGO not only exhibits lower electrical resistance and higher sensitivity but also possesses enhanced semiconductor properties. The oxygen functional groups present in rGO act as active binding sites for gas molecules, significantly improving adsorption activity. Moreover, rGO demonstrates high thermal stability, a large surface area, and excellent mechanical strength, making it an ideal candidate for gas sensing applications. In addition to carbon-based materials, nanostructures, including semiconductor metal oxides (ZnO, TiO_2) and metal nanoparticles (Ag, Au), have also been widely studied for their effectiveness in various sensing applications [8–12].

* Corresponding authors.
E-mail addresses: tlchang@ntnu.edu.tw (T.-L. Chang), tsf@ntut.edu.tw (S.-F. Tseng), shuhanhsu@siit.tu.ac.th (S.-H. Hsu).

https://doi.org/10.1016/j.apsusc.2026.166898
Received 23 February 2026; Received in revised form 9 April 2026; Accepted 13 April 2026
Available online 15 April 2026
0169-4332/© 2026 Published by Elsevier B.V.

The combination of rGO with metal oxides, such as titanium dioxide (TiO_2), further enhances gas sensor performance. TiO_2, an n-type semiconductor with a wide band gap (3.2 eV), is known for its chemical stability and low cost but suffers from high charge carrier recombination rates. Under ultraviolet (UV) irradiation, TiO_2 generates photoinduced electron-hole pairs, which can interact with adsorbed gas molecules, enhancing the response and sensitivity of the sensor [13]. When combined with p-type rGO, a p-n junction is formed, which adjusts the space charge layer at the interface, improving charge separation and transport. The work function difference between TiO_2 (4.20 eV) and rGO (4.60 eV) facilitates electron transfer from TiO_2 to rGO, enhancing conductivity and sensitivity. Moreover, rGO provides a conductive network that accelerates electron transfer, while TiO_2 serves as a reaction center for adsorbed gases [14]. This synergistic effect enhances the gas sensing capabilities of the composite, making it highly effective for detecting gases such as CO.

In recent decades, laser processing has advanced rapidly, demonstrating great potential for surface modification and the fabrication of micro-nano structures [15,16]. Compared with continuous wavelength (CW) laser and long pulse laser, femtosecond laser (Fs-laser) has emerged as a critical ability in precision surface manufacturing due to its ultra-short pulses, high peak power, and minimal thermal effect [17–20]. Its minimal thermal effect can prevent heat accumulation, allowing precise control over material structures and properties, while its non-contact manufacturing process minimizes contamination and preserves material integrity. In gas sensing applications, Fs-laser processing can be used to reduce GO into rGO films [21,22]. While laser-induced graphene (LIG) directly converted from polyimide (PI) or other carbon precursors has emerged as a powerful platform for gas sensors [23,24], such processes typically rely on the localized ablation and carbonization of the substrate itself. In contrast, this study utilizes the Fs-laser to precisely reduce a pre-coated TiO_2/GO composite film. Because the laser energy is primarily absorbed by the GO matrix to form rGO, this one-step, non-contact and low-thermal-effect process patterns the conductive electrode structures entirely within the composite layer, without causing ablation or structural damage to the underlying flexible substrate. Consequently, this methodology not only facilitates the synergistic integration of TiO_2 for UV-enhanced CO sensing but also offers high versatility, as it can be applied to various heat-sensitive flexible substrates without being limited to PI.

In this study, Fs-laser processing was employed to simultaneously reduce GO to rGO and to directly pattern TiO_2/rGO composite microelectrodes on a flexible PI substrate. A uniform TiO_2/GO thin film was first deposited by spin-coating, and the laser processing enabled precise structural modification without significant substrate damage. Leveraging the photocatalytic properties of TiO_2, known for its high catalytic activity and chemical stability [25], the sensing measurements were conducted at room temperature (25 °C) under a controlled relative humidity of 30% to minimize cross-interference caused by the competitive adsorption of ambient water molecules. As extensively reported in previous studies, traditional TiO_2-based gas sensors typically require elevated operating temperatures (e.g., 400–600 °C) to provide sufficient thermal activation energy for effectively detecting CO gas [26]. However, this high-temperature requirement severely limits their integration into heat-sensitive flexible platforms. To overcome this limitation, our study utilized UV illumination at room temperature to generate photogenerated charge carriers, effectively replacing the need for thermal activation [27]. This room temperature operability provides a significant advantage by substantially reducing power consumption and ensuring safe integration into flexible platforms. The fabricated sensor demonstrated a notable response of 20% to 150 ppm CO with a rapid response time of less than 15 sec. Moreover, under 365 nm UV irradiation, the synergistic photocatalytic activity of TiO_2 enhances the sensing response. These findings demonstrate that Fs-laser processing provides a simple and effective route for fabricating TiO_2/rGO composites with UV-enhanced gas sensing performance, offering a promising approach for flexible, high-performance CO sensors and next-generation wearable or environmental monitoring devices.

2. Experimental

2.1. Fabrication of flexible TiO_2/rGO composite sensor via femtosecond laser processing

The procedure to prepare the TiO_2/rGO composite electrode via FS-laser processing was described as follows. In this study, rutile TiO_2 (R-900, Emperor Chemical Corporation, Taiwan), was selected as the base material for the gas sensor. The coating solution was prepared by dispersing TiO_2 powder at concentrations of 2 wt%, 5 wt%, and 10 wt% in 2.5 mg/ml GO solution (EW-GO-S, EWAY technology Corporation, Taiwan) labeled as GT-2, GT-5, GT-10 (detailed values are listed in Table S1). The mixture was thoroughly stirred to obtain a uniform TiO_2/GO composite solution

Fig. 1 shows the schematic of the fabrication process for the flexible CO gas sensor. The PI substrate (PIF175, Mortech Corporation, Taiwan), was cut to dimensions of 15 mm × 15 mm × 0.175 mm. It was thoroughly rinsed with deionized water (DI water) to remove impurities and then dried to eliminate surface moisture. The TiO_2/GO composite solution was then evenly coated onto the PI substrate using spin coating technology at a rotation speed of 2000 rpm and 30 sec. Finally, the coated substrate was cured on a hot plate at 60 °C for 90 min to remove residual solvent and ensure firm adhesion of the film to the substrate.

The high resistance of the TiO_2/GO composite hindered practical resistance measurements; thus, one-step Fs-laser processing was employed to structurally modify the composite. The experimental setup consisted of an Fs-laser source (Spirit HE 1040–30-SHG, Spectra Physics, USA), integrated with an XY-axis scanner (intelliSCAN III 10, SCANLAB GmbH, Germany). A 520 nm wavelength laser was used, with parameters optimized at a scanning speed of 50 mm/sec and a fluence of 0.34 J/cm^2. The composite was scanned once by the laser at a repetition rate of 100 kHz, thereby reducing the GO in the TiO_2/GO composite to rGO, as shown in Fig. 1a. The laser induce TiO_2/rGO composites were labeled as rGT-2, rGT-5, and rGT-10, corresponding to the TiO_2 weight percentages. Finally, the design of the ring electrode facilitated uniform 365 nm UV illumination with an intensity of 6.96 mW/cm^2 (5H1U1, Yi-Lian Electronics Technology Co., Ltd., Taiwan), thereby enhancing the performance of the UV-assisted flexible CO gas sensor. The design of the sensor electrode is illustrated in Fig. S1.

This study used a source measure unit to record the electrical changes of the sensor under different concentrations of gas at a frequency of every 0.1 sec. Gas sensing performance was evaluated in terms of response and sensitivity. Among them, the gas response refers to the gain between the input signal and the output signal of the probe system. The equation used is shown in the following:

$$Response(\%) = \frac{R_a - R_g}{R_a} \times 100 \quad (1)$$

where R_a is the resistance in air and R_g is the resistance in the target gas.

It is defined as the ratio of the sensor resistance value in the air environment to the sensor resistance value when gas is introduced. The absolute value after subtracting the resistance value of the sensor in the air environment (R_a) from the resistance value in the gas (R_g) is divided by R_a (Eq. (1). In this study, the reactivity of the sensor was evaluated under ambient atmospheric conditions to simulate practical operation. The tests were performed in a sealed transparent acrylic chamber with a volume of 1 L, which allowed UV light to irradiate the sensor surface during gas detection. To control the gas concentration, a static volumetric method was employed. Specifically, calculated volumes of CO gas (99.9%, Air Products and Chemicals, Inc., Taiwan) were directly injected into the air-filled chamber to achieve the target parts per million (ppm) levels. The target gas was allowed to diffuse and mix with the

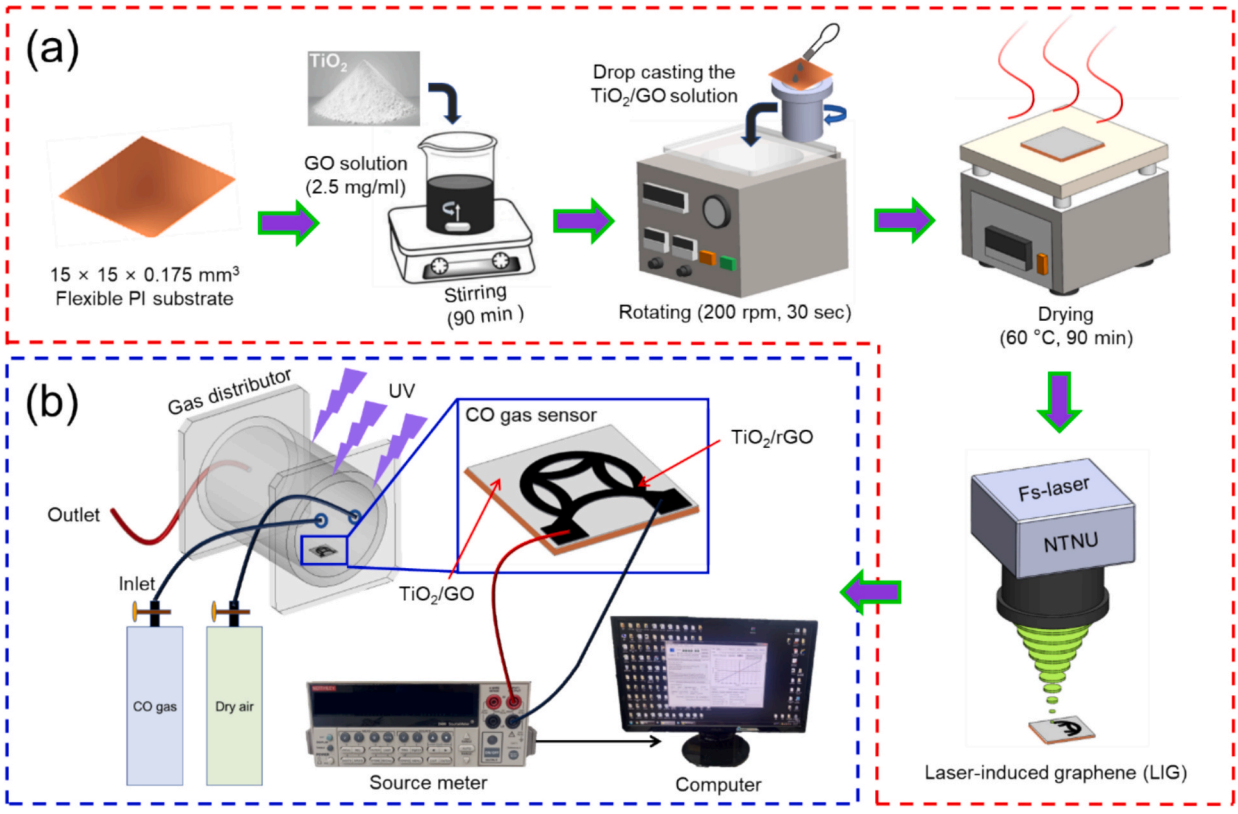


Fig. 1. (a) Schematic illustration of the fabrication process for the flexible CO gas sensor. (b) Schematic diagram of a room temperature flexible CO gas sensor.

ambient air within the sealed environment while the electrical response was monitored. Furthermore, all sensing measurements were conducted at room temperature (25 °C) under a controlled relative humidity of 30%, as shown in Fig. 1b.

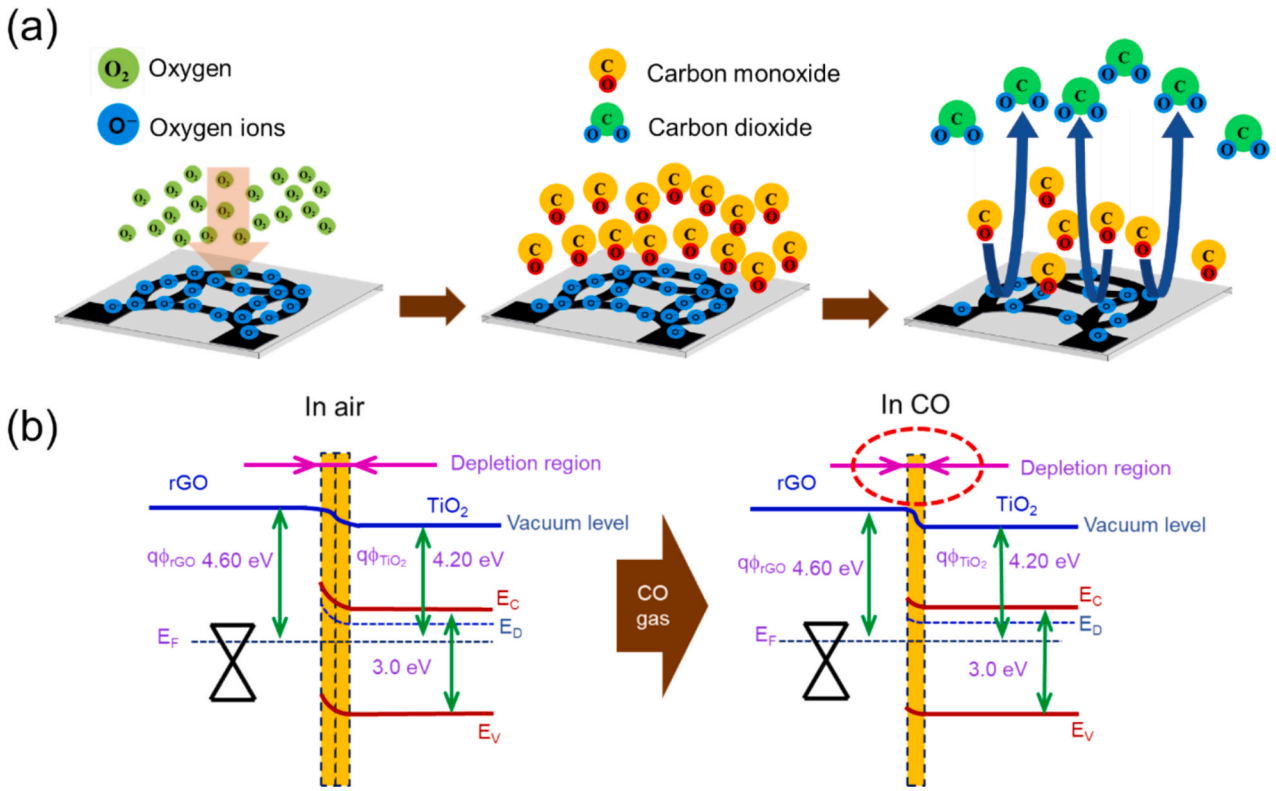


Fig. 2. (a) CO gas sensing mechanism, and (b) energy band diagram of the TiO_2/rGO composite during gas sensing.

2.2. Sensing mechanism

This study investigated the sensing of CO gas using a TiO_2/rGO composite sensor. While TiO_2 is widely known to respond to various gases, CO was selected as a representative target gas due to its environmental importance and its well-established interaction with metal oxide-based sensing materials. In addition, previous studies have reported that rGO-based materials exhibit high sensitivity to CO at room temperature [28], making it suitable for evaluating the sensing performance of TiO_2/rGO composites. By integrating TiO_2 with rGO, the composite enables synergistic effects in charge transfer and surface adsorption, leading to an enhanced sensing response toward CO. Based on this synergistic interaction, the CO sensing process of our composite can be described by four key reactions. Initially, the sensor was exposed to air within a cavity, allowing oxygen molecules to absorb onto the surface of the TiO_2/rGO composite. When a voltage was applied to the sensing structure, the surface of the sensor becames more electronegative. The oxygen adsorbed by the sensor extracts electrons from it and ionizes it into O^-, O^{2-} (Eq. 2–3). Upon exposure to CO, the gas reacted with these oxygen ions, removing them from the TiO_2/rGO surface and producing CO_2 along with excess electrons. The CO_2 gas and excess electrons produced by chemical reactions will desorbed into the air. Therefore, when the CO gas was turned on, a significant decrease in the resistance value of the sensor was observed.

As illustrated in Fig. 2a, CO molecules react with pre-adsorbed oxygen ions on the TiO_2/rGO surface, forming CO_2 through surface oxidation. This process underlies the sensing mechanism of the TiO_2/rGO composite, where charge transfer and surface reactions govern the resistance change during CO detection. As a result, the CO concentration decreases while the CO_2 concentration increases (Eq. 4–5) [27].

$$O_{2(gas)} + 2e^- \rightarrow 2O^-_{(ads)} \tag{2}$$

$$\frac{1}{2}O_{2(gas)} + 2e^- \rightarrow O^{2-}_{(ads)} \tag{3}$$

$$CO_{(gas)} + O^-_{(ads)} \rightarrow CO_{2(gas)} + e^- \tag{4}$$

$$CO_{(gas)} + O^{2-}_{(ads)} \rightarrow CO_{2(gas)} + 2e^- \tag{5}$$

The primary reason for the resistance reduction in the CO gas sensor was the increase in free electron concentration. CO underwent a redox reaction with surface-adsorbed oxygen ions, releasing electrons back into the conduction band of TiO_2. This process increased the free electron concentration in the conduction band, thereby reducing the resistance of TiO_2, as electrons were the majority carriers in the n-type semiconductor. Additionally, the reduction in surface-adsorbed oxygen ions led to a shrinkage of the depletion region, further decreasing the resistance. Simultaneously, the reaction between CO and oxygen ions altered the charge distribution on the TiO_2 surface, reducing electron trapping at the interface, which also contributed to the resistance reduction [29], as illustrated in Fig. 2b. The magnitude of the work function could influence the adsorption capacity of oxygen ions and the efficiency of electron trapping. In this study, TiO_2 had a smaller work function compared to rGO. This allowed electrons to more easily transfer from TiO_2 to surface-adsorbed oxygen molecules, forming more oxygen ions and enhancing the sensitivity of the sensor. However, in the mechanism where CO removed surface-adsorbed oxygen ions, the surface redox reaction was the dominant factor, and the influence of the work function was relatively secondary.

2.3. Characterization

The thickness of the sensing film was estimated to be approximately 20 μm using optical microscopy (OM, BX51, Olympus, Japan). Surface morphology of the TiO_2/GO and TiO_2/rGO composite films before and after femtosecond laser processing was observed by scanning electron microscopy (SEM, JSM-7600F, JEOL, Japan), while elemental composition and oxidation states were analyzed using energy-dispersive X-ray spectroscopy (EDS, Oxford X-Max, Oxford Instruments, UK) equipped with the SEM system. Crystal phase identification and changes induced by laser reduction were investigated by X-ray diffraction (XRD, D8 Advance Plus, Bruker, USA) using Cu Kα1 radiation ($\lambda = 1.5406$ Å), with the tube operated at 40 kV and 40 mA. The reduction degree of graphene oxide and characteristic carbon vibrational modes were further confirmed by micro-Raman identify spectrometer (MRI, MRI532S, ProTrusTech, Taiwan) using a 532 nm excitation laser. Surface chemical states and the reduction degree of graphene oxide were examined by X-ray photoelectron spectroscopy (XPS, JPS-9030, JEOL, Japan), with all binding energies calibrated to the adventitious C 1 s peak at 284.8 eV. Functional groups in the composites were characterized by Fourier transform infrared spectroscopy (FTIR, Bruker ALPHA FTIR spectrometer, Bruker, Germany) in attenuated total reflectance (ATR) mode over the wavenumber range of 400–4000 cm^{-1}. Optical absorption properties were measured using an ultraviolet–visible-near infrared spectrophotometer (UV–Vis, V670, Jasco, Japan) in the wavelength range of 200–800 nm. Electrical resistance and gas sensing performance were recorded using a source measure unit (Keithley 2400, Keithley Instruments, USA) with a data acquisition interval of 0.1 sec.

3. Results and discussion

3.1. Femtosecond laser induced reduction TiO_2/rGO composite

This study used Fs-laser processing to induced the reduction of TiO_2/GO film into TiO_2/rGO composite in a single process. As shown in Fig. 3a, the sheet resistance of the 2 wt% TiO_2/GO film continuously decreased from 1.28 MΩ to 592 kΩ as the fluence was raised to 0.34 J/cm^2, indicating that a higher energy density promoted more complete photothermal reduction and the formation of a conductive TiO_2/rGO composite. However, when the fluence exceeded 0.34 J/cm^2, the resistance began to rise, most likely owing to local overheating that induced partial re-oxidation [30]. Hence, 0.34 J/cm^2 was identified as the optimum fluence for subsequent processing. At this optimum fluence, the post-reduction resistance increased linearly with TiO_2 loading from 2 wt % to 10 wt% ($R^2 = 0.9048$), as presented in Fig. 3b, confirming that excessive TiO_2 content reduces the overall conductivity of the composite. The EDS analysis further verified the compositional changes after Fs-laser reduction, as shown in Fig. 3c (Fig. S2, Table S2), revealing the removal of oxygen species and the formation of TiO_2/rGO heterostructures (TiO_2/rGO composite).

The surface morphology after Fs-laser processing was examined using SEM. The micrographs shown in Fig. 3d reveal the initial GO film surface before reduction, which appeared smooth and compact with a dense sheet-like morphology. In addition, it was observed that the laser-induced rGO morphology with a single scanning direction and varying laser fluence to optimize the laser parameters to form significant rGO surface. Here, the laser parameters of the study were fixed at a repetition rate of 100 kHz and a scanning speed of 50 mm/sec. The effect of changing fluence on the resistance value of the rGO film was discussed, and the lowest resistance value measured was considered the optimal laser fluence. It was worth mentioning that the resistance value decreases as the fluence increases, indicating that the laser induces the formation of rGO on the surface of the GO film. The lowest resistance value of 3.1 kΩ was achieved at a fluence of 0.34 J/cm^2, which was identified as the optimal laser fluence for preparing rGO. Herein the induced rGO film exhibits a layered structure as a result of the combined photothermal and photochemical effects generated by Fs-laser irradiation [31,32]. As seen in Fig. 3e, the SEM micrograph of the rGO film clearly shows wrinkled, flaky, and porous surface morphologies. When the laser fluence was further increased, the resistance began to rise.

Further morphological analyses of the TiO_2/GO and TiO_2/rGO composites are presented in Fig. 3f and Fig. 3g, respectively. The TiO_2/

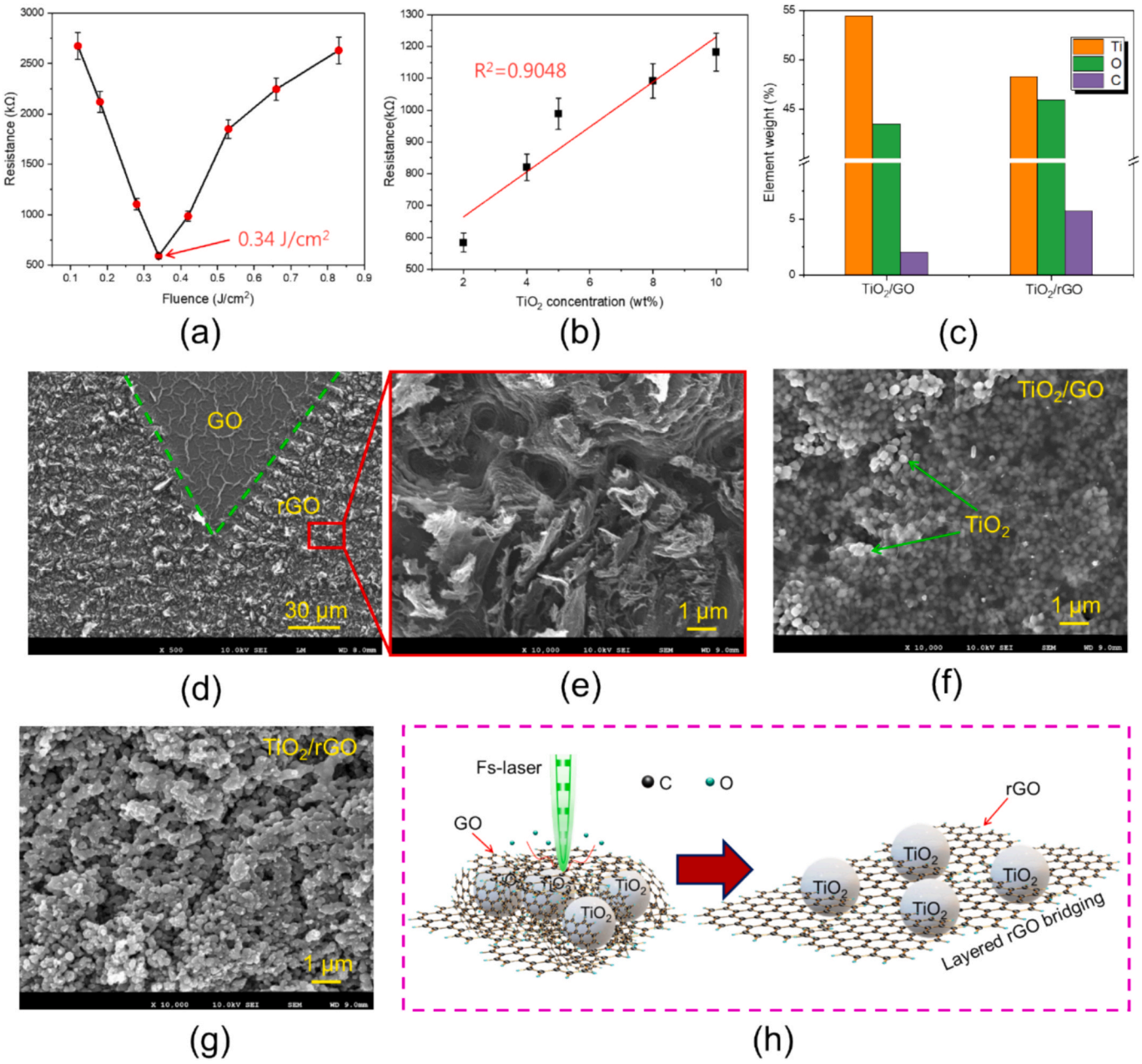


Fig. 3. (a) Variation of resistance with laser fluence for laser induced reduction GO film. (b) Resistance of TiO_2/rGO composite with different concentrations at a fluence of 0.34 J/cm^2. (c) Elemental composition of TiO_2/GO and TiO_2/rGO determined by EDS analysis. SEM images of (d) GO and rGO film, (e) rGO film, (f) TiO_2/GO composite film, (g) TiO_2/rGO composite film. (h) Schematic illustration of GO wrapping TiO_2 before and layered TiO_2/rGO composite after Fs-laser induced reduction.

GO composite exhibited TiO_2 nanoparticles uniformly embedded and coated by the GO matrix, forming a continuous hybrid film. After laser reduction, the TiO_2/rGO composite showed a more distinct layered structure, in which rGO sheets were interlaced with TiO_2 particles. The SEM image in Fig. 3g clearly reveals that the TiO_2 nanoparticles were uniformly distributed and tightly anchored within the rGO network, forming conductive pathways that facilitate efficient electron transport. These features indicate the successful reduction and structural reorganization of the composite. Such morphological observations are consistent with the proposed structural evolution model illustrated in Fig. 3h. The schematic shows the transformation from the initial GO-encapsulated TiO_2 configuration to the layered TiO_2/rGO composite formed through Fs-laser-induced reduction. This hierarchical structure enhances interfacial contact between TiO_2 and rGO, providing continuous charge transport channels that improve electrical conductivity and contribute to superior gas-sensing performance.

It is important to emphasize that a key advantage of the proposed Fs-laser approach is its ability to fabricate sensing structures while minimizing damage to the underlying flexible substrate. Unlike conventional LIG processes that required the destructive ablation and carbonization of the PI substrate itself, our process localized the photothermal and photochemical effects primarily within the pre-coated TiO_2/GO layer. Furthermore, this maskless direct-writing process provided exceptional versatility in electrode design. Because the conductive pathways were directly drawn by the laser, sensing electrodes of any customized shape or dimension could be effortlessly patterned without the constraints of traditional photolithography or physical masks. More importantly, this non-destructive nature eliminated the dependency on specific substrate

materials such as PI. As a result, the process can be extended to a broader range of flexible or heat-sensitive substrates. Consequently, this method enables one-step material reduction and electrode patterning while preserving the structural integrity of the underlying flexible substrate.

3.2. Phase and structural characterization of the composites

The XRD patterns of the TiO_2/GO and laser-processed TiO_2/rGO composite films are presented in Fig. 4a. Both samples display the characteristic signatures of the rutile TiO_2 phase (JCPDS No. 21-1276), with intense diffraction peaks located at $2\theta = 27.4°$, 36.1°, 41.2°, and 54.3°, corresponding to the (1 1 0), (1 0 1), (1 1 1), and (2 1 1) planes, respectively [33,34]. This high crystallinity confirms that the femtosecond laser irradiation (0.34 J/cm^2) preserved the structural integrity of the TiO_2 lattice without inducing amorphization. Regarding the carbonaceous component, the expected broad (002) peak of rGO is not distinctly visible. This is attributed to the shielding effect of the adjacent, high-intensity TiO_2 (1 1 0) peak, as the atomic scattering factor of titanium is significantly higher than that of carbon [35].

In this study, Raman spectroscopy was employed to corroborate the phase composition and structural evolution of the composite induced by femtosecond laser irradiation. The spectra provided critical insight into the phonon vibrational dynamics of the TiO_2 lattice and the reorganization of the carbon network, as shown in Fig. 4b. In the low-frequency region (<800 cm^{-1}), the characteristic phonon modes of the rutile TiO_2 phase were clearly identified. The peaks located at approximately 143 cm^{-1}, 447 cm^{-1}, and 612 cm^{-1} corresponded to the B_{1g}, E_g, and A_{1g} active modes, respectively [36]. In the pristine TiO_2/GO spectrum, these TiO_2 signatures were relatively weak. This suppressed intensity was attributed to the shielding effect of the thick, oxygen-rich GO layers wrapping the nanoparticles and the associated fluorescence background. However, after laser treatment, the intensity of the TiO_2 peaks, particularly the E_g and A_{1g} modes, was significantly enhanced. This phenomenon was attributed to two concurrent processes: the laser-induced removal of the amorphous oxygenated carbon overlay, and the localized photothermal annealing. These processes improved the crystallinity of the TiO_2 nanoparticles, thereby increasing their Raman scattering cross-section.

In the high-frequency region, the structural quality of the carbon network was evaluated through the D band (~1352 cm^{-1}) and the G band (~1596 cm^{-1}). Physically, the G band corresponds to the in-plane bond stretching motion of sp^2 carbon atoms, while the D band originates from the breathing mode of sp^2 rings, which is activated only in the presence of defects. The intensity ratio of the D band to the G band (I_D/I_G) served as a key metric for defect density and graphitic ordering. The I_D/I_G ratio decreased from 1.05 in the precursor TiO_2/GO film to 0.98 in the laser-processed TiO_2/rGO composite [37]. These results indicate that the reduction in the I_D/I_G ratio provided direct evidence of a synergistic mechanism. The high-intensity Fs-laser triggered the multi-photon reduction of oxygen-containing functional groups, while the subsequent non-radiative relaxation generated localized heat that annealed the carbon lattice. This process effectively healed the structural defects and partially restored the conjugated sp^2 graphitic network [38]. Consequently, the Fs-laser processing not only reduced the GO, but also reconstructed the conductive pathways essential for the performance of the composite.

3.3. XPS analysis

XPS was performed to investigate the surface chemical states of the Fs-laser-induced TiO_2/rGO composite, as shown in Fig. S3. The C 1 s spectrum of GT-5 exhibited a dominant sp^2-C═C/sp^3-C–C component accompanied by several oxygen-containing groups (C–O, C═O, and O–C═O) [39]. After Fs-laser induced, rGT-5 showed an increased sp^2-C═C contribution and a pronounced decrease in oxygen-bonded components [40,41], as shown in Fig. 5a, b. This variation indicates that the laser treatment effectively removed oxygen-containing groups and restored the conjugated carbon network, indicating successful reduction of GO to rGO.

In the Ti 2p region, no obvious Ti signal was detected in GT-5, which was likely due to the complete coverage of TiO_2 nanoparticles by the GO overlayer [42]. The thick GO film strongly attenuated the photoelectrons emitted from the underlying Ti atoms, resulting in the absence of detectable Ti 2p peaks. After laser irradiation, weak but clear Ti $2p_{3/2}$ and Ti $2p_{1/2}$ peaks appeared at approximately 458.5 eV in rGT-5, as shown in Fig. 5c, d. The emergence of these signals suggests that the Fs-laser locally thinned or ablated the GO layer and partially exposed the buried TiO_2 domains, allowing the Ti signal to be detected by XPS [43].

The O 1 s spectra further support this interpretation. GT-5 was mainly composed of C═O/Ti-OH/defect-related oxygen species with minor adsorbed oxygen [44]. After laser reduction, rGT-5 exhibited an increased proportion of lattice/defect oxygen and a decrease in adsorbed oxygen. These results imply that the Fs-laser removed surface adsorbates and generated oxygen vacancies in the TiO_2 lattice [45]. The formation

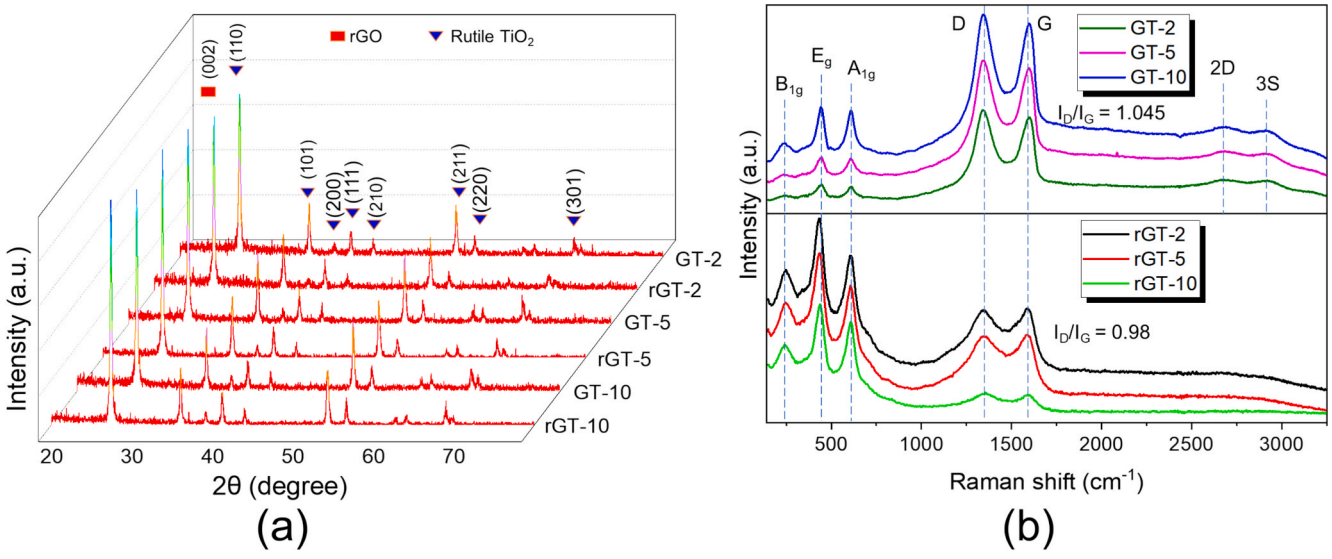


Fig. 4. (a) XRD pattern of the TiO_2/GO composite ; (b) Raman spectra of the corresponding films, showing the characteristic TiO_2 modes and the D/G bands of the carbon network.

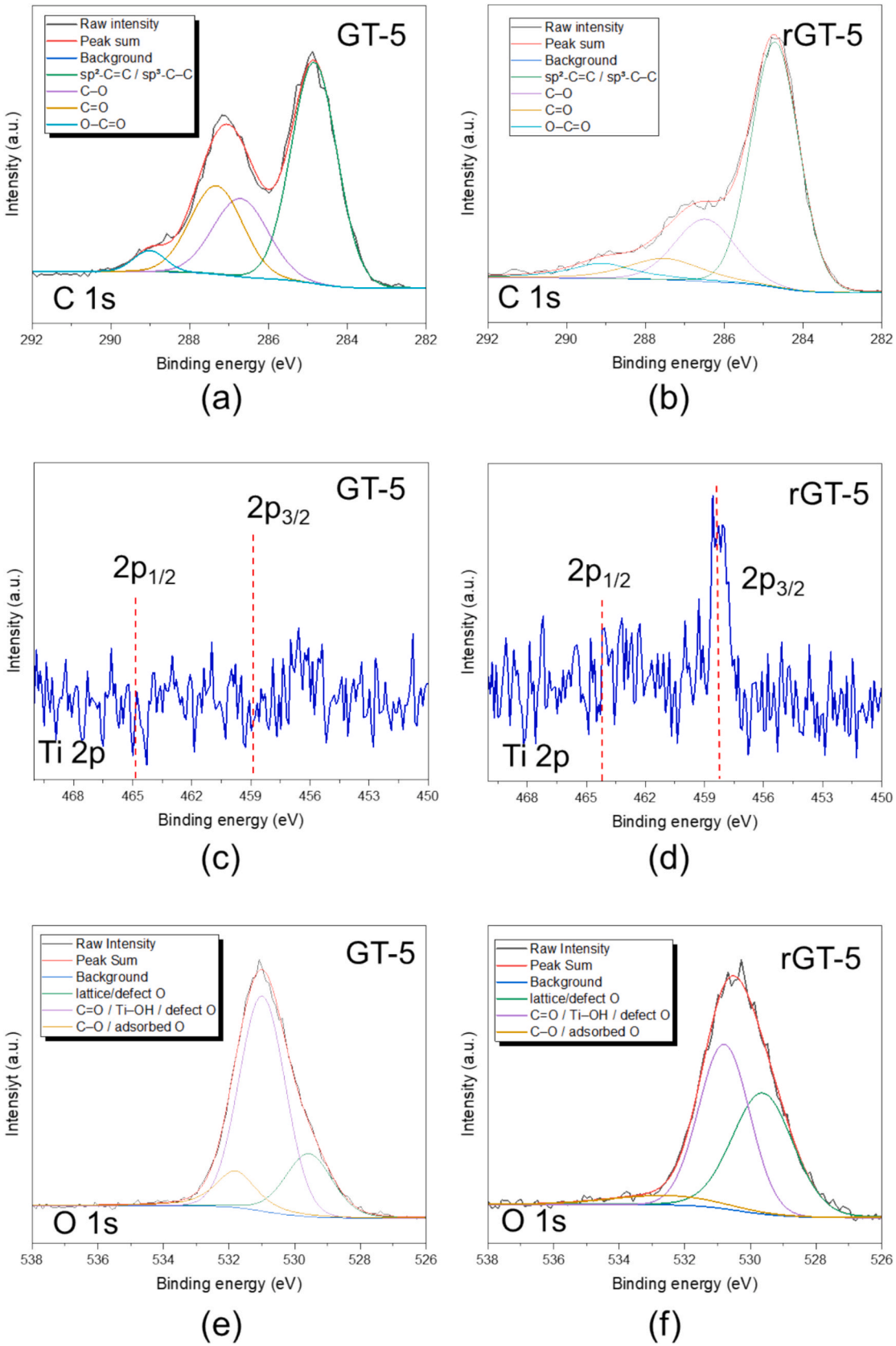


Fig. 5. XPS analysis of the GT-5 and rGT-5 composites. C 1 s spectra of (a) GT-5, and (b) rGT-5 ; Ti 2p spectra of (a) GT-5, and (b) rGT-5 ; The O 1 s spectra of (a) GT-5, and (b) rGT-5.

of oxygen defects and the exposure of TiO_2 domains are expected to facilitate charge transfer across the TiO_2/rGO interface, which can contribute to the enhancement of gas sensing performance, as presented in Fig. 5e-5f.

These findings demonstrate that Fs-laser processing not only promotes GO reduction but also induces oxygen-deficient TiO_2 domains, providing favorable electronic and chemical conditions for improved CO sensing performance. The detailed XPS quantitative results are summarized in Table S3.

3.4. FTIR and UV–VIS analysis and bending test

This study used FTIR to analyze the material properties of composite. All GT samples exhibited characteristic peaks corresponding to the C═C skeletal vibration of the aromatic ring (~1600 cm^{-1}), the C-O stretching vibration of hydroxyl or epoxy groups (~1220 cm^{-1}), and the Ti-O stretching vibration of the TiO_2 phase (~750 cm^{-1}). After Fs-laser induced, the samples (rGT-2, rGT-5, rGT-10) exhibited a noticeable decrease in the intensity of the C-O peak and a relative enhancement of the C═C peak [46]. This change indicates that oxygen-containing groups on GO were removed and the conjugated sp^2 carbon network was partially restored, confirming the laser-induced reduction of GO to rGO. Meanwhile, the Ti-O vibration peak remained visible, suggesting that the embedded TiO_2 structure was retained after laser processing [47], as shown in Fig. 6a.

To evaluate the UV light absorption capability of the composite used in this study, the absorption spectra were measured using UV–VIS. All samples exhibited strong absorption in the UV region, which gradually decreased toward the visible region. A distinct absorption edge was observed at around 365 nm, corresponding to the bandgap transition of TiO_2. Compared with the samples before laser reduction, the Fs-laser induce reduction samples (rGT-2, rGT-5, rGT-10) exhibited slightly enhanced absorption in the visible region. This enhancement can be attributed to the restoration of the sp^2-conjugated domains and the generation of oxygen vacancies, which introduce localized states within the bandgap and improve light absorption [48]. These results indicate that the Fs-laser not only reduced GO but also modulated the optical properties of the TiO_2/rGO composites, as shown in Fig. 6b.

To evaluate mechanical flexibility and durability under repeated deformation, a bending test was performed on rGT-5. This test aimed to determine whether sensing performance remains stable under mechanical stress, which is important for applications in wearable or flexible electronics. rGT-5 was fixed at a 90° bending angle with a bending radius of approximately 1 cm, and a pneumatic reciprocating mechanism applied continuous bending cycles while electrical resistance was monitored. After more than 50 cycles, resistance remained below 40 kΩ, indicating stable performance and no significant structural damage, as shown in Fig. 6c. These results confirm that bending deformation does not affect function. The bending test setup of the flexible TiO_2/rGO composite CO gas sensor is shown in Fig. 6d. Variation of resistance of the rGT-5 sensor under different bending angles (0°, 30°, 60°, and 90°). It was found that bending the sensor would reduce the resistance stability. The resistance increased slightly with increasing bending angle, showing a good linear correlation (R^2 = 0.9766), as shown in Fig. 6e. The gas response of the sensor to 150 ppm CO was measured at 25 °C under different bending angles. Experimental results showed that when the bending angle was 0°, the response value was 15.1%, while it further decreased to 8.2% at 90°. It was observed that at smaller angles (such as 0° and 30°), the response was almost unaffected; however, as the angle increased, the response showed a clear decreasing trend. This decrease occurred because the effective surface area of the sensing material on the flexible electrode was reduced during bending, which lowered the ability to adsorb gas molecules and capture electrons, leading to a lower sensing response, as shown in Fig. 6f. Consequently, the study not only verifies the structural robustness under bending stress but also highlights the potential of this approach for developing wearable gas sensors that maintain stable operation in dynamic environments. Such characteristics are essential for future integration into flexible electronics and real-time environmental monitoring systems.

3.5. CO gas sensing

The gas sensing characteristics of the TiO_2/rGO composites were further explored. Fig. 7 describes the gas sensors made with different weight percentages of TiO_2 for different concentrations of CO gas sensing. The sensing measurements were conducted at 25 °C under a controlled relative humidity of 30%. This specific humidity level was maintained to minimize potential interference from ambient moisture. As reported in previous studies [49,50], humidity generally affects the gas-sensing performance of metal oxide-based sensors. This behavior is primarily attributed to the competitive adsorption between water molecules and the target gas (CO). Water molecules tend to occupy active surface sites, thereby reducing the available adsorption sites for CO and leading to a decreased sensing response. Therefore, a controlled humidity condition (30% RH) was adopted to provide a consistent baseline for evaluating the intrinsic sensing performance of the TiO_2/rGO composite. When CO gas was passed through the sensor, the CO gas removed oxygen ions from the TiO_2/rGO composites. This causes the resistance of the sensor to drop. Use rGT-2 sensor. The resistance before CO gas enters was 592 kΩ. When the rGT-2 sensor was placed in a 150 ppm CO gas environment. The resistance drops sharply, with a response time of < 10 sec, and when the CO gas concentration continues to rise, the resistance drops even more dramatically. The response reaches 29.1% at 500 ppm.

The resistance of rGT-5 was 988 kΩ in air. The rGT-5 sensor has a similar gas response to the rGT-2 sensor when different concentrations of CO gas were introduced. The increase in resistance was due to the decrease in the proportion of conductive rGO. If the TiO_2 ratio was further increased to 10 wt%, the resistance of the rGT-10 sensor in air increased significantly to 1182 kΩ. Relatively, the CO gas sensing response was also improved to 39.5% at 500 ppm (detailed values are listed in Table 1), as shown in Fig. 7a. To investigate the role of UV activation, the electrical and sensing characteristics were systematically analyzed. As observed in the transient resistance measurements (Fig. 7b), UV irradiation significantly reduced the baseline resistance of the sensors. This phenomenon is attributed to the generation of electron-hole pairs on the TiO_2 surface, which increases carrier concentration and effectively lowers the impedance to a measurable range suitable for practical sensing circuits. Fig. 7c quantifies this photo-induced resistance drop, defined as $\Delta R_{UV} = R_{off} - R_{on}$, under different UV wavelengths. The results indicate that the rGT-10 sensor exhibited the most substantial resistance reduction, particularly under 365 nm excitation, demonstrating the most effective charge transfer within the composite network (detailed values are listed in Table 2). Regarding the gas sensing performance, Fig. 7d presents the response as a function of CO concentration. To evaluate the reproducibility of the sensors, each concentration point was tested multiple times (n ≧ 5). The small standard deviations demonstrate the excellent reproducibility of the fabricated devices, which is inherently guaranteed by the highly precise and programmable Fs-laser direct-writing process. It is noteworthy that while the primary contribution of UV irradiation was the modulation of baseline resistance, it provided only a moderate enhancement in sensitivity rather than a drastic change. Specifically, the response of the rGT-10 sensor towards 500 ppm CO increased from 39.6% (Without UV) to 43.8% (With 365 UV). This suggests that UV activation can establish a low-resistance conduction path beneficial for signal acquisition without altering the fundamental interaction mechanism between the sensor and the target gas.

Given that the sensor operated at 25 °C, the influence of environmental humidity was considered a critical factor for practical applications. The dynamic response of the rGT-5 sensor under varying relative humidity (RH) levels ranging from 30% to 95%. A stepwise and reversible decrease in resistance was observed as the RH increased

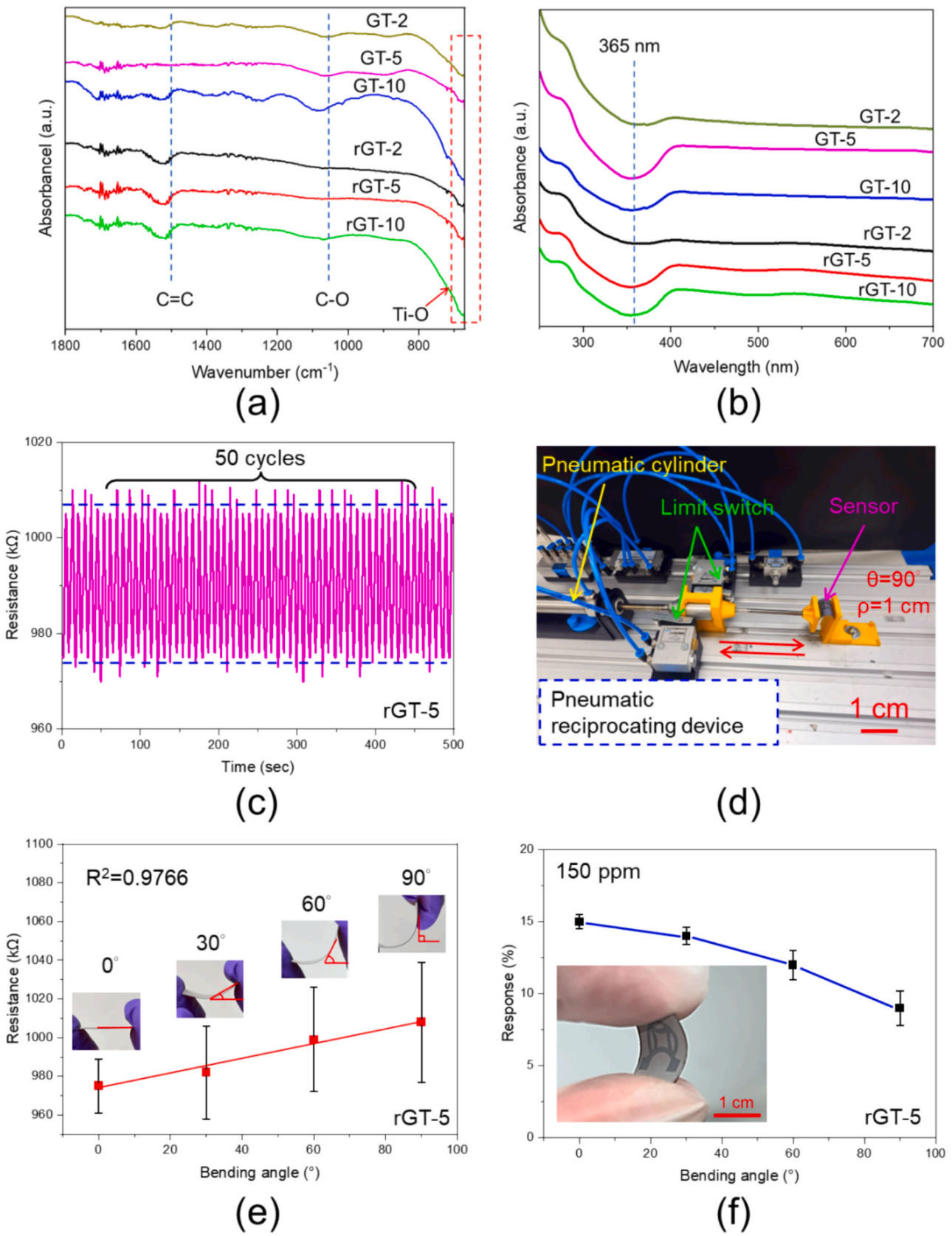


Fig. 6. (a) FTIR spectra showing decreased C-O and enhanced C=C peaks after laser induced, indicating GO reduction, while Ti-O remained. (b) UV–VIS spectra showing an absorption edge near 365 nm from TiO_2, with slightly increased visible absorption in laser-reduced samples. (c) Flexible CO gas sensor repeated b00ending tests at 90°. (d) Flexible gas sensor bending test setup and entity. (e) Resistance of the rGT-5 sensor under different bending angles. (f) The gas response of the sensor to 150 ppm CO was measured under different bending angles.

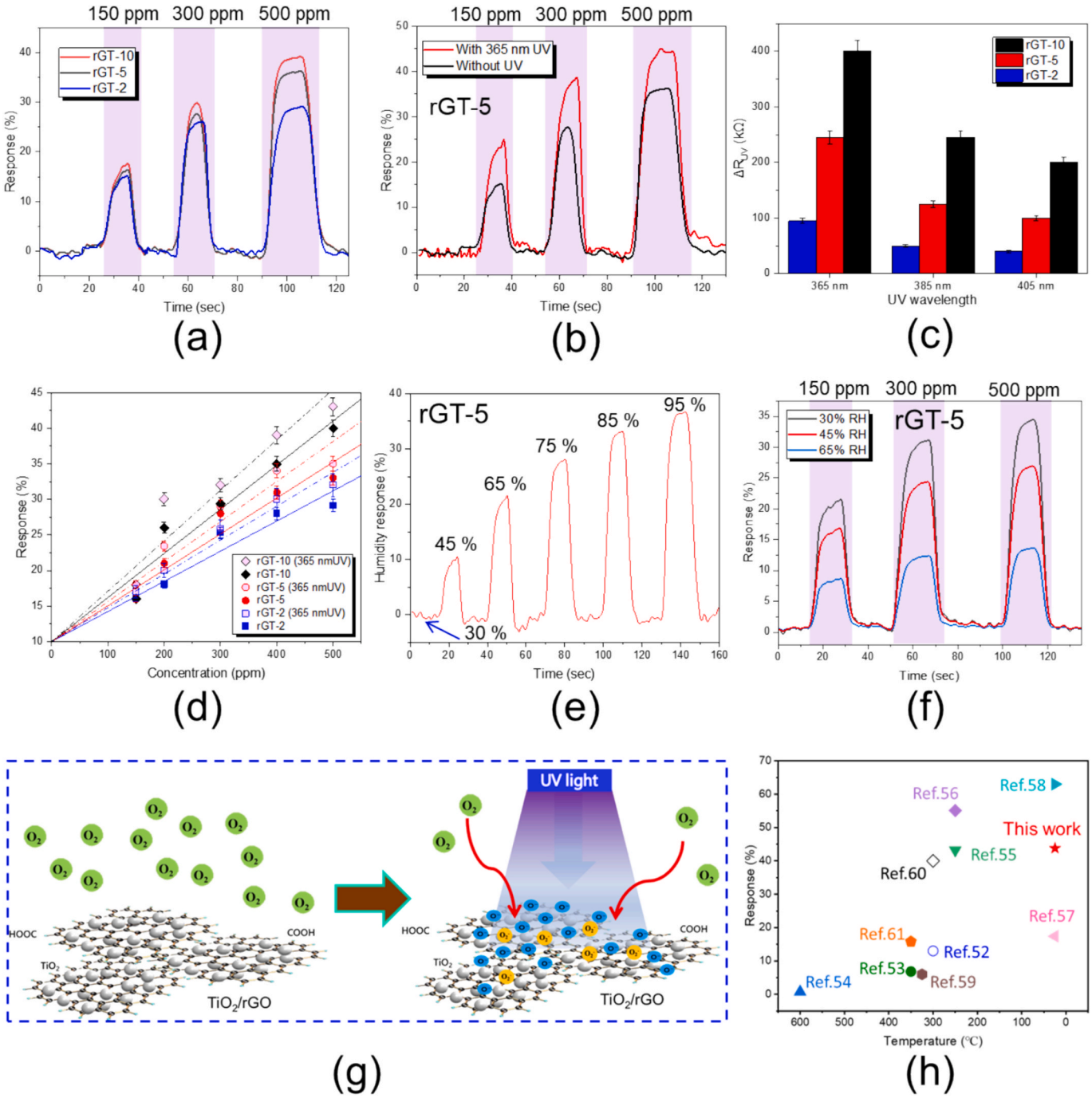


Fig. 7. (a) Responses of TiO_2/rGO sensors under different CO concentrations. (b) Comparison of gas sensing responses with and without UV light irradiation (c) Resistance changes of TiO_2/rGO sensors under different UV wavelengths. (d) The gas response comparison. (e) Humidity response. (f) Gas sensing response under different humidity. (g) Schematic diagram mechanism of UV light on composite. (h) Comparison of the response and temperature of composite fabricated in this study with those reported in previous studies.

incrementally to 30%, 45%, 66%, 75%, 85%, and 95%, as shown in Fig. 7e. This trend was attributed to the ionic conduction facilitated by physisorbed water molecules on the composite surface, which enhanced charge transport. More critically, the capability of the sensor to detect CO gas in high-humidity environments was evaluated. Although a slight attenuation in response was observed due to the competitive adsorption between water molecules and CO gas for surface active sites, the sensor maintained a robust detection capability, as shown in Fig. 7f.

The sensing mechanism of the TiO_2/rGO composite under UV illumination is illustrated in Fig. 7g. Under 365 nm UV light, TiO_2 generates photoinduced electron–hole pairs that participate in interfacial charge transfer processes, influencing the overall sensing behavior. Here, adsorbed oxygen molecules captured electrons, forming reactive oxygen ions (O^-, O_2^-), which reduced the space charge layer (Eq. 6–7) [51].

$$TiO_2/rGO + h\nu \rightarrow TiO_2(h^+) + rGO(e^-) \quad (6)$$

$$rGO(e^-) + O_2 \rightarrow rGO + O_2^- \quad (7)$$

The photogenerated electrons migrate from the TiO_2 conduction band to the rGO surface due to the work function difference between the two materials, while the holes remain in TiO_2 and participate in oxidation reactions. Meanwhile, absorbed oxygen molecules on the

Table 1
Comparison of CO gas sensing responses of TiO_2/rGO composites with different TiO_2 contents.

Composite composition	UV (365 nm)	Initial resistance (kΩ)	CO gas concentration (ppm)	Final resistance (kΩ)	Response (%)	Response time/Recovery time
rGT-2	off	592	150	497	15.8	3/4
			300	447	24.5	5/4
			500	420	29.1	7/8
	on	497	150	412	17.1	3/4
			300	372	25.1	5/5
			500	338	31.9	6/ 8
rGT-5	off	988	150	832	16.0	3/4
			300	715	27.6	5/4
			500	654	33.8	7/8
	on	745	150	610	18.1	5/5
			300	531	28.7	5/4
			500	484	35.0	7/7
rGT-10	off	1182	150	973	17.6	3/4
			300	813	31.2	5/4
			500	714	39.6	7/8
	on	782	150	641	18	3/3
			300	532	31.9	5/6
			500	439	43.8	7/8

Table 2
Comparison of TiO_2/rGO composites under UV irradiation.

Composite composition	Initial resistance (kΩ)	UV wavelength (nm)	Final resistance (kΩ)	ΔR_{UV}(kΩ)	UV Response (%)	Response time/Recovery time
rGT-2	592	365	497	95	16.0	6/8
		385	541	47	7.9	9/7
		405	554	38	6.4	11/6
rGT-5	988	365	745	243	24.6	6/9
		385	863	125	12.7	8/8
		405	890	98	9.9	11/7
rGT10	1182	365	782	400	33.8	4/10
		385	937	245	20.7	6/8
		405	980	202	17.0	9/8

composite surface capture the transferred electrons to form reactive oxygen ions (O^- and O_2^-), which modulate the surface charge layer and influence the sensor resistance. The work function difference facilitated electron transfer from TiO_2 to rGO, enhancing conductivity and decreasing overall resistance. Under CO exposure, CO molecules react with these oxygen ions, releasing trapped electrons back into the TiO_2/rGO network. This process increases the carrier concentration, reduces the depletion region, and results in a decrease in overall resistance. The synergistic effect of UV-induced charge separation in TiO_2 and the high conductivity of rGO enhances interfacial electron transfer, thereby improving the CO sensing performance of the composite sensor.

To evaluate the effectiveness of the Fs-laser fabricated TiO_2/rGO sensor, its CO sensing performance was compared with previously reported TiO_2-based sensors. As summarized in Table 3, most TiO_2-based CO sensors reported in previous studies relied on high-temperature operation to achieve moderate responses. Electrospun nanofibers [52], sol–gel films [53], and sintered xerogels [54] exhibited responses of only 0.7–13% at operating temperatures between 300 and 600 °C. Structural modifications, such as hollow hemispheres [55] and ZnO hybridization [56], improved the sensing response but still required temperatures above 250 °C and suffered from long recovery times (>70 s). In contrast, the present TiO_2/rGO composite sensor demonstrates a significant response to CO at room temperature, indicating the effectiveness of the Fs-laser fabricated flexible sensing platform. Room temperature strategies, including Co_3O_4/Y_2O_3 or Mg doping [57,58] and MWCNT incorporation [61], have been developed to reduce power consumption; however, these approaches often sacrifice mechanical flexibility or involve complex, multi-step fabrication. By contrast, the Fs-laser induced TiO_2/rGO composite developed in this study achieved a 43.8% response with symmetric 5 sec/5 sec dynamics at room temperature on a bendable PI substrate. This performance rivals that of Mg-doped TiO_2 thin films (63% at 25 °C) while being realized through an one-step laser process. Furthermore, under 365 nm UV irradiation, the overall resistance decreased, facilitating charge transfer and enhancing

Table 3
Comparison of the response characteristics of gas sensors reported in previous studies.

Material	Gas	Response (%)	Response time/ Recovery time	Operating temperature (℃)	Fabrication	Substrate material	Reference
TiO_2 nanofiber	CO	13	5/6	300 °C	Electrospinning	Silicon	[52]
TiO_2 film	CO	6.81	5/92	350 °C	Sol-gel synthesis	Silicon	[53]
TiO_2 film	CO	0.74	20/70	600 °C	Calcination and sintering	Alumina	[54]
TiO_2 HH	CO	43.2	10/10	250 °C	Templating and calcination	SiO_2/Si	[55]
TiO_2 /ZnO	CO	55.1	10/100~	250 °C	Thermal oxidation	Alumina	[56]
$Co_3O_4/TiO_2/Y_2O_3$	CO	17.4	120/60	RT	Reaction kettle	Glass	[57]
Mg/TiO_2	CO	63	41/22	RT	Sol-gel synthesis	Silicon	[58]
Au/ TiO_2	CO	6	5/8	325 °C	Hydrothermal	Al_2O_3	[59]
TiO_2 /CeO_2	CO	40	2/6	300 ℃	Hydrothermal	$CeOHCO_3$	[60]
TiO_2/MWCNT	CO	15.8	4/16	350 °C	Sol-gel synthesis	Silicon	[61]
TiO_2/rGO	**CO**	**43.8**	**<10/<10**	**RT**	**Fs-laser**	**PI**	**This work**

HH = hollow hemispheres, MWCNT = multiwalled carbon nanotubes, RT = room temperature (25 °C).

sensing performance. These results indicate that rGO incorporation and laser-assisted reduction effectively lowered the activation barrier for CO chemisorption, while the synergistic photocatalytic effect of TiO_2 under UV irradiation further improved sensitivity, enabling fast, low-power, and flexible CO detection. Comparison with previously reported the response and temperature of composite, as shown in Fig. 7h.

4. Conclusion

In summary, a room temperature flexible CO gas sensor based on a TiO_2/rGO composite was successfully fabricated via using a one-step femtosecond (Fs) laser-induced and patterning process. The ultrafast laser simultaneously reduced the TiO_2/GO thin film and directly patterned electrodes on a PI substrate under optimized parameters (100 kHz repetition rate, 50 mm/sec scanning speed, and 0.34 J/cm^2 fluence), achieving precise material modification with minimal substrate damage. Consequently, the sensor exhibited a high response of 43.8% toward 500 ppm CO with a rapid response time of less than 10 sec. Under 365 nm UV irradiation, the photocatalytic activity of TiO_2 further enhanced sensing performance by decreasing the overall resistance. Moreover, the device maintained excellent mechanical stability, showing consistent electrical characteristics with an average resistance of 40 kΩ after multiple bending cycles. The remarkable improvement in gas sensing performance can be attributed to the synergistic effects of rGO incorporation, laser-induced oxygen vacancies, and the photocatalytic properties of TiO_2 under UV light, which collectively facilitate charge transfer and gas adsorption at the TiO_2/rGO interface. Importantly, this room temperature operability successfully overcomes the conventional high-temperature requirement of metal oxide sensors, significantly reducing power consumption and greatly expanding its application scope for wearable devices and multi-scenario deployments. Therefore, this study demonstrates an effective one-step Fs-laser strategy for fabricating UV-enhanced TiO_2/rGO flexible gas sensors and provides a promising route for developing high-performance, low-power, and wearable sensing platforms for real-time environmental monitoring.

CRediT authorship contribution statement

Yuan-Jun Chen: Writing – original draft, Methodology, Formal analysis, Data curation, Conceptualization. **Tien-Li Chang:** Writing – original draft, Supervision, Methodology, Funding acquisition, Conceptualization. **Shih-Feng Tseng:** Validation, Supervision, Investigation, Conceptualization. **Wen-Tse Hsiao:** Validation, Resources, Investigation, Formal analysis. **Shu-Han Hsu:** Validation, Supervision, Investigation, Conceptualization.

Declaration of competing interest

The authors declare that they have no known competing financial interests or personal relationships that could have appeared to influence the work reported in this paper.

Acknowledgments

The authors acknowledge the support by the National Science and Technology Council, Republic of China (Taiwan) under grant numbers 114-2221-E-003-009-MY2, 114-2622-E-003-001, 113-2622-E-003-002, and 111-2221-E-003-008-MY3. This work was also supported by the Higher Education Sprout Project of National Taiwan Normal University and the Ministry of Education (MOE), Taiwan.

Appendix A. Supplementary data

Supplementary data to this article can be found online at https://doi.org/10.1016/j.apsusc.2026.166898.

Data availability

Data will be made available on request.

References

[1] J.H. Kim, J.Y. Kim, A. Mirzaei, H.W. Kim, S.S. Kim, Synergistic effects of SnO_2 and Au nanoparticles decorated on WS_2 nanosheets for flexible, room-temperature CO gas sensing, Sens. Actuators B 332 (2021) 129493, https://doi.org/10.1016/j.snb.2021.129493.
[2] G. Can, U. Sayılı, Ö. Aksu Sayman, Ö.F. Kuyumcu, D. Yılmaz, E. Esen, E. Yurtseven, E. Erginöz, Mapping of carbon monoxide related death risk in Turkey: a ten-year analysis based on news agency records, BMC Public Health 19 (2019) 9, https://doi.org/10.1186/s12889-018-6342-4.
[3] R.W. Byard, Carbon monoxide – the silent killer, Forensic Sci. Med. Pathol. 15 (2018) 1–2, https://doi.org/10.1007/s12024-018-0040-5.
[4] L. Barret, V. Danel, J. Faure, Carbon monoxide poisoning, a diagnosis frequently overlooked, J. Toxicol. Clin. Toxicol. 23 (1985) 309–313, https://doi.org/10.3109/15563658508990638.
[5] T. Shimazu, Half-life of Blood Carboxyhemoglobin, Chest 119 (2001) 661–662, https://doi.org/10.1378/chest.119.2.661.
[6] S. Basu, P. Bhattacharyya, Recent developments on graphene and graphene oxide based solid state gas sensors, Sens. Actuators B 173 (2012) 1–21, https://doi.org/10.1016/j.snb.2012.07.092.
[7] P. Recum, T. Hirsch, Graphene-based chemiresistive gas sensors, Nanoscale Adv. 6 (2024) 11–31, https://doi.org/10.1039/d3na00423f.
[8] G. Jung, S. Hong, Y. Jeong, W. Shin, J. Park, D. Kim, J.H. Lee, Highly selective and low-power carbon monoxide gas sensor based on the chain reaction of oxygen and carbon monoxide to WO_3, ACS Appl. Mater. Interfaces 14 (2022) 17950–17958, https://doi.org/10.1021/acsami.1c25221.
[9] C. Qin, B. Wang, N. Wu, C. Han, C. Wu, X. Zhang, Q. Tian, S. Shen, P. Li, Y. Wang, Metal-organic frameworks derived porous Co_3O_4 dodecahedrons with abundant active Co3+ for ppb-level CO gas sensing, Appl. Surf. Sci. 506 (2020) 144900, https://doi.org/10.1016/j.apsusc.2019.144900.
[10] M.S. Yang, S.K. Bae, D.B. Seo, K. Lee, Y. Son, S.H. Kim, J.H. Jung, K.S. An, I. Park, J.H. Seo, Facile formation of nanoporous reduced graphene oxide via epoxy-based negative photoresist laser irradiation for highly sensitive and selective gas detection, Sens. Actuators B 426 (2025) 137073, https://doi.org/10.1016/j.snb.2024.137073.
[11] A. Khan, F. Ameen, F. Khan, A. Al-Arfaj, B. Ahmed, Fabrication and antibacterial activity of nanoenhanced conjugate of silver (I) oxide with graphene oxide, Mater. Today Commun. 25 (2020) 101667, https://doi.org/10.1016/j.mtcomm.2020.101667.
[12] Z. Nezafat, B. Feizi Mohazzab, B. Jaleh, M. Nasrollahzadeh, T. Baran, M. Shokouhimehr, A promising nanocatalyst: Upgraded Kraft lignin by titania and palladium nanoparticles for organic dyes reduction, Inorg. Chem. Commun. 130 (2021) 108746, https://doi.org/10.1016/j.inoche.2021.108746.
[13] Z. Li, H. Huang, D. Zhao, S. Chen, W. Cai, T. Tang, UV-activated room temperature oxygen gas sensor based on TiO_2-decorated bridging GaN nanowires, Sens. Actuators B 401 (2024) 135015, https://doi.org/10.1016/j.snb.2023.135015.
[14] P.N.O. Gillespie, N. Martsinovich, Origin of charge trapping in TiO_2/reduced graphene oxide photocatalytic composites: insights from theory, ACS Appl. Mater. Interfaces 11 (2019) 31909–31922, https://doi.org/10.1021/acsami.9b09235.
[15] V.L. Lagunov, M. Rybachuk, A. Itthagarun, L.J. Walsh, R. George, Modification of dental enamel, dentin by an ultra-fast femtosecond laser irradiation: a systematic review, Opt. Laser Technol. 155 (2022) 108439, https://doi.org/10.1016/j.optlastec.2022.108439.
[16] H. Wang, F. Zhang, J. Duan, Bioinspired broadband and mechanically-durable infrared antireflective subwavelength array by temporal-spatial shaping femtosecond laser micromachining, Chem. Eng. J. 506 (2025) 159928, https://doi.org/10.1016/j.cej.2025.159928.
[17] Y. Tao, Y. Ren, X. Wang, R. Zhao, J. Liu, C. Deng, C. Wang, W. Zhang, H. Hao, A femtosecond laser-assembled SnO_2 microbridge on interdigitated Au electrodes for gas sensing, Mater. Lett. 308 (2022) 131120, https://doi.org/10.1016/j.matlet.2021.131120.
[18] J. Zhu, Q. Li, Q. Chen, B. Liu, Z. Wei, Precise and smooth structure on InP fabricated by femtosecond laser direct writing-assisted wet etching, Opt. Laser Technol. 176 (2024) 110944, https://doi.org/10.1016/j.optlastec.2024.110944.
[19] J. Yong, Q. Yang, X. Hou, F. Chen, Nature-inspired superwettability achieved by femtosecond lasers, Ultrafast Sci. 2022 (2022), https://doi.org/10.34133/2022/9895418.
[20] H. Zhu, Y.Z. Dai, X.C. Sun, H. Xia, A fine single Pd microwire H_2 sensor fabricated by using a femtosecond laser for a wide detection range at room temperature, Nanoscale Adv. 4 (2022) 4162–4168, https://doi.org/10.1039/d2na00462c.
[21] L. Wang, Y. Ding, J. Li, Y. Guan, L. Yang, H. Fang, X. Lv, J. Yuan, Femtosecond laser induced one-step nanopatterning and preparation of rGO/RuO_2 electrodes for high-performance micro-supercapacitors, J. Electroanal. Chem. 919 (2022) 116501, https://doi.org/10.1016/j.jelechem.2022.116501.
[22] Z. Zhai, Y. Qu, Y. Zhang, N. Wu, M. Yin, Y. Cui, Preparation and performance of rGO coating on C/C composite finger seal with femtosecond laser, Mater. Lett. 312 (2022) 131685, https://doi.org/10.1016/j.matlet.2022.131685.
[23] J. Zhao, N. Yi, X. Ding, S. Liu, J. Zhu, A.C. Castonguay, Y. Gao, L.D. Zarzar, H. Cheng, In situ laser-assisted synthesis and patterning of graphene foam

composites as a flexible gas sensing platform, Chem. Eng. J. 456 (2023) 140956, https://doi.org/10.1016/j.cej.2022.140956.
[24] C. Kim, H.K. Nam, M. Kang, T. Jing, K. Lee, D. Yang, J.H. Ha, Y. Kwon, Y. Lee, Y. J. Kim, I. Park, Wooden green multi-gas sensors with femtosecond laser-induced graphene for sustainable environmental monitoring, Chem. Eng. J. 530 (2026) 173407, https://doi.org/10.1016/j.cej.2026.173407.
[25] M. Al-Hashem, S. Akbar, P. Morris, Role of oxygen vacancies in nanostructured metal-oxide gas sensors: a review, Sens. Actuators B 301 (2019) 126845, https://doi.org/10.1016/j.snb.2019.126845.
[26] J. Zhao, H. Wang, Y. Cai, J. Zhao, Z. Gao, Y.Y. Song, The challenges and opportunities for tio$_2$ nanostructures in gas sensing, ACS Sensors 9 (2024) 1644–1655, https://doi.org/10.1021/acssensors.4c00137.
[27] H. He, J. Guo, J. Zhao, J. Xu, C. Zhao, Z. Gao, Y.Y. Song, Engineering CuMOF in TiO_2 nanochannels as Flexible Gas Sensor for High-Performance NO detection at room temperature, ACS Sensors 7 (2022) 2750–2758, https://doi.org/10.1021/acssensors.2c01318.
[28] D. Panda, A. Nandi, S.K. Datta, H. Saha, S. Majumdar, Selective detection of carbon monoxide (CO) gas by reduced graphene oxide (rGO) at room temperature, RSC Adv. 6 (2016) 47337–47348, https://doi.org/10.1039/c6ra06058g.
[29] H.G. Pozos, K.T.V. Krishna, M. de la Luz Olvera, Y. Amador, A.M. Kudriavtsev, Alvarez, TiO_2 thin film based gas sensors for CO-detection, J. Mater. Sci. Mater. Electron. 29 (2018) 15829–15837, https://doi.org/10.1007/s10854-018-9477-2.
[30] S. Movaghgharnezhad, P. Kang, Laser-induced graphene: synthesis advances, structural tailoring, enhanced properties, and sensing applications, J. Mater. Chem. C 12 (2024) 6718–6742, https://doi.org/10.1039/d3tc04677j.
[31] S. Kang, C.C. Evans, S. Shukla, O. Reshef, E. Mazur, Patterning and reduction of graphene oxide using femtosecond-laser irradiation, Opt. Laser Technol. 103 (2018) 340–345, https://doi.org/10.1016/j.optlastec.2018.01.059.
[32] X. Ye, Z. Yang, X. Zheng, H. Qiang, M. Wei, Y. Li, M. Chen, N. Luo, A review on the laser-induced synthesis of graphene and its applications in sensors, J. Mater. Sci. 59 (2024) 11644–11668, https://doi.org/10.1007/s10853-024-09883-z.
[33] D.A.H. Hanaor, C.C. Sorrell, Review of the anatase to rutile phase transformation, J. Mater. Sci. 46 (2010) 855–874, https://doi.org/10.1007/s10853-010-5113-0.
[34] K. Zhou, Y. Zhu, X. Yang, X. Jiang, C. Li, Preparation of graphene–TiO_2composites with enhanced photocatalytic activity, New J. Chem. 35 (2011) 353–359, https://doi.org/10.1039/c0nj00623h.
[35] A.R. Ansari, S.A. Ansari, N. Parveen, M.O. Ansari, Z. Osman, Silver nanoparticles decorated on the surface of reduced graphene oxide coated titanium oxide nanocomposite for enhanced electrochemical supercapacitance performance, Ionics 28 (2022) 4793–4804, https://doi.org/10.1007/s11581-022-04685-2.
[36] L. Kernazhitsky, V. Shymanovska, T. Gavrilko, V. Naumov, L. Fedorenko, V. Kshnyakin, J. Baran, Photoluminescence of Cr-doped TiO_2 induced by intense UV laser excitation, J. Lumin. 166 (2015) 253–258, https://doi.org/10.1016/j.jlumin.2015.03.034.
[37] G. Gao, Q. Zhu, H. Chong, J. Zheng, C. Fan, G. Li, Synthesis of biphasic defective TiO_{2-x}/reduced graphene oxide nanocomposites with highly enhanced photocatalytic activity, Chem. Res. Chin. Univ. 34 (2018) 158–163, https://doi.org/10.1007/s40242-018-7369-x.
[38] A.B. Suriani, A. Mohamed Muqoyyanah, M.H.D. Othman, M.H. Mamat, N. Hashim, M.K. Ahmad, N. Nayan, H.P.S.A. Khalil, Reduced graphene oxide-multiwalled carbon nanotubes hybrid film with low Pt loading as counter electrode for improved photovoltaic performance of dye-sensitised solar cells, J. Mater. Sci. Mater. Electron. 29 (2018) 10723–10743, https://doi.org/10.1007/s10854-018-9139-4.
[39] T. Zou, B. Zhao, W. Xin, Y. Wang, B. Wang, X. Zheng, H. Xie, Z. Zhang, J. Yang, C. Guo, High-speed femtosecond laser plasmonic lithography and reduction of graphene oxide for anisotropic photoresponse, Light Sci. Appl. 9 (2020) 69, https://doi.org/10.1038/s41377-020-0311-2.
[40] M. Kasischke, S. Maragkaki, S. Volz, A. Ostendorf, E.L. Gurevich, Simultaneous nanopatterning and reduction of graphene oxide by femtosecond laser pulses, Appl. Surf. Sci. 445 (2018) 197–203, https://doi.org/10.1016/j.apsusc.2018.03.086.
[41] Z. Wan, S. Wang, B. Haylock, J. Kaur, P. Tanner, D. Thiel, R. Sang, I.S. Cole, X. Li, M. Lobino, Q. Li, Tuning the sub-processes in laser reduction of graphene oxide by adjusting the power and scanning speed of laser, Carbon 141 (2019) 83–91, https://doi.org/10.1016/j.carbon.2018.09.030.
[42] A. Jablonski, C.J. Powell, Effective attenuation lengths for different quantitative applications of X-ray photoelectron spectroscopy, J. Phys. Chem. Ref. Data 49 (2020) 033102, https://doi.org/10.1063/5.0008576.
[43] R.S. Weatherup, B. Eren, Y. Hao, H. Bluhm, M.B. Salmeron, Graphene membranes for atmospheric pressure photoelectron spectroscopy, J. Phys. Chem. Lett. 7 (2016) 1622–1627, https://doi.org/10.1021/acs.jpclett.6b00640.
[44] M. Tošić, V. Rajić, D. Pjević, S. Stojadinović, N. Krstulović, S. Dimitrijević-Branković, M. Momčilović, Synergy of Nd:YAG picosecond pulsed laser irradiation and electrochemical anodization in the formation of TiO_2 nanostructures for the photocatalytic degradation of pesticide carbofuran, Photonics 11 (2024) 284, https://doi.org/10.3390/photonics11030284.
[45] B. Bharti, S. Kumar, H.N. Lee, R. Kumar, Formation of oxygen vacancies and Ti3+ state in TiO_2 thin film and enhanced optical properties by air plasma treatment, Sci. Rep. 6 (2016) 32355, https://doi.org/10.1038/srep32355.
[46] F. Ghasemi, S. Razi, K. Madanipour, Single-step laser-assisted graphene oxide reduction and nonlinear optical properties exploration via CW laser excitation, J. Electron. Mater. 47 (2018) 2871–2879, https://doi.org/10.1007/s11664-018-6133-9.
[47] W.K.C. Yung, G. Li, H.M. Liem, H.S. Choy, Z. Cai, Eye-friendly reduced graphene oxide circuits with nonlinear optical transparency on flexible poly(ethylene terephthalate) substrates, J. Mater. Chem. C 3 (2015) 11294–11299, https://doi.org/10.1039/c5tc02405f.
[48] S.A. Balsamo, R. Fiorenza, M. Condorelli, R. Pecoraro, M.V. Brundo, F. Lo Presti, S. Sciré, One-pot synthesis of TiO_2-rGO photocatalysts for the degradation of groundwater pollutants, Materials 14 (2021) 5938, https://doi.org/10.3390/ma14205938.
[49] Y. Wang, Y. Zhou, Recent progress on anti-humidity strategies of chemiresistive gas sensors, Materials 15 (2022) 8728, https://doi.org/10.3390/ma15248728.
[50] S. Wicker, M. Guiltat, U. Weimar, A. Hémeryck, N. Barsan, Ambient humidity influence on CO detection with SnO_2 gas sensing materials. A combined DRIFTS/DFT investigation, J. Phys. Chem. C 121 (2017) 25064–25073, https://doi.org/10.1021/acs.jpcc.7b06253.
[51] R. Saha, A. Neha, A. Thukral, P.S. Pal, Sunlight responsive superhydrophilic rGO-TiO2 nanocomposite coatings for photovoltaic applications, Diam. Relat. Mater. 149 (2024) 111603, https://doi.org/10.1016/j.diamond.2024.111603.
[52] A. Nikfarjam, S. Hosseini, N. Salehifar, Fabrication of a highly sensitive single aligned TiO_2 and gold nanoparticle embedded TiO_2 nano-fiber gas sensor, ACS Appl. Mater. Interfaces 9 (2017) 15662–15671, https://doi.org/10.1021/acsami.6b15554.
[53] J.S. Lee, T.J. Ha, M.H. Hong, H.H. Park, The effect of porosity on the CO sensing properties of TiO_2 xerogel thin films, Thin Solid Films 529 (2013) 98–102, https://doi.org/10.1016/j.tsf.2012.10.072.
[54] Z.M. Seeley, A. Bandyopadhyay, S. Bose, Influence of crystallinity on CO gas sensing for TiO_2 films, Mater. Sci. Eng. B 164 (2009) 38–43, https://doi.org/10.1016/j.mseb.2009.06.009.
[55] H.G. Moon, Y.S. Shim, H.W. Jang, J.S. Kim, K.J. Choi, C.Y. Kang, J.W. Choi, H. H. Park, S.J. Yoon, Highly sensitive CO sensors based on cross-linked TiO_2 hollow hemispheres, Sens. Actuators B 149 (2010) 116–121, https://doi.org/10.1016/j.snb.2010.06.014.
[56] T. Santhaveesuk, K. Shimanoe, K. Suematsu, S. Choopun, Size-independent and ultrahigh CO gas sensor based on TiO_2 modified ZnO tetrapods, Phys. Status Solidi (a) 215 (2018) 1700784, https://doi.org/10.1002/pssa.201700784.
[57] S. Li, J. Pu, S. Zhu, Y. Gui, Co_3O_4@TiO_2@Y_2O_3 nanocomposites for a highly sensitive CO gas sensor and quantitative analysis, J. Hazard. Mater. 422 (2022) 126880, https://doi.org/10.1016/j.jhazmat.2021.126880.
[58] M. Kumar, A.K. Gupta, D. Kumar, Mg-doped TiO_2 thin films deposited by low cost technique for CO gas monitoring, Ceram. Int. 42 (2016) 405–410, https://doi.org/10.1016/j.ceramint.2015.08.124.
[59] H. Liu, W. Yang, M. Wang, L. Xiao, S. Liu, Fabrication of lotus-like Au@TiO_2 nanocomposites with enhanced gas-sensing properties, Sens. Actuators B 236 (2016) 490–498, https://doi.org/10.1016/j.snb.2016.06.039.
[60] B. Chen, P. Li, B. Wang, Y. Wang, Flame-annealed porous TiO_2/CeO_2 nanosheets for enhanced CO gas sensors, Appl. Surf. Sci. 593 (2022) 153418, https://doi.org/10.1016/j.apsusc.2022.153418.
[61] J.S. Lee, T.J. Ha, M.H. Hong, C.S. Park, H.H. Park, The effect of multiwalled carbon nanotube doping on the CO gas sensitivity of TiO_2 xerogel composite film, Appl. Surf. Sci. 269 (2013) 125–128, https://doi.org/10.1016/j.apsusc.2012.10.020.